# Excited-State Geometry Optimization with the Density Matrix Renormalization Group, as Applied to Polyenes

Weifeng Hu and Garnet Kin-Lic Chan*

Department of Chemistry, Princeton University, Princeton, New Jersey 08544, United States

S Supporting Information

ABSTRACT: We describe and extend the formalism of state-specific analytic density matrix renormalization group (DMRG) energy gradients, first used by Liu et al. [*J. Chem. Theor. Comput.* **2013**, *9*, 4462]. We introduce a DMRG wave function maximum overlap following technique to facilitate state-specific DMRG excited-state optimization. Using DMRG configuration interaction (DMRG-CI) gradients, we relax the low-lying singlet states of a series of *trans*-polyenes up to $C_{20}H_{22}$. Using the relaxed excited-state geometries, as well as correlation functions, we elucidate the exciton, soliton, and bimagnon ("single-fission") character of the excited states, and find evidence for a planar conical intersection.
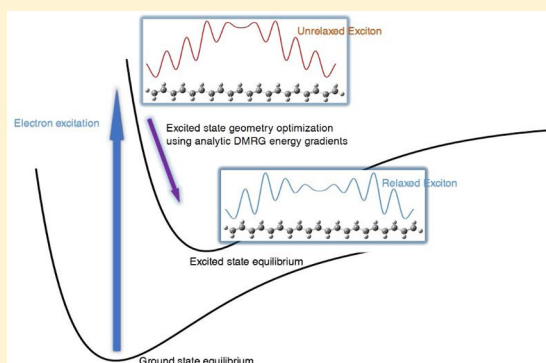
1. INTRODUCTION

The density matrix renormalization group,[1−15] introduced by White,[1] has made large active space multireference quantum chemistry calculations routine. In the context of chemistry, there have been many improvements to White's algorithm, including orbital optimization,[16−19] spin adaptation,[20−22] dynamic correlation treatments,[23−25] and response theories,[26,27] to name a few. The density matrix renormalization group (DMRG) has been applied in many different electronic structure problems, ranging from benchmark exact solutions of the Schrödinger equation for small molecules,[5,25,28−31] to active space studies of conjugated π-electron systems,[32−35] the elucidation of the ground and excited states of multicenter transition-metal clusters,[36−41] computation of high-order correlation contributions to the binding energy of molecular crystals,[42] relativistic calculations,[43] and the study of curve crossings in photochemistry.[44]

Energy gradients are crucial to electronic structure as they define equilibrium structures, transition states, and reaction trajectories. Analytic energy gradients, introduced by Pulay,[45−48] are preferred to numerical gradients, because of their low cost and numerical stability, and are now implemented for many single- and multireference quantum chemistry methods.[49−55]

Analytic DMRG energy gradients were first used by Liu et al.[44] in a study of the photochromic ring opening of spiropyran. The theory, although simple, was not fully discussed. A contribution of the current work is to provide a more complete exposition of the theory behind DMRG gradients. A second contribution is to discuss their practical implementation in excited-state geometry optimization. The simplest formulation of the gradients arises when the excited states are treated in a state-specific manner (that is, without orthogonality constraints

to lower states). However, such DMRG calculations can be susceptible to root flipping, for example, near conical intersections. Furthermore, DMRG wave functions are specified both by a choice of active space as well as by discrete sets of quantum numbers associated with each orbital (used to enforce global symmetries, such as the total particle number). During an energy minimization, it is important that the wave function changes smoothly. Here, we present a state-specific DMRG analytic gradient algorithm that uses a maximum overlap technique both to stably converge excited states, and to ensure adiabatic changes of both the orbitals and the DMRG wave function during geometry changes.

Trans-polyenes are well-known examples of molecules with interesting ground- and excited state structure, and they form the central motifs for a large set of of biological compounds, such as retinals and the carotenoids. Many calculations using semiempirical models (such as the Pariser−Parr−Pople (PPP) model) as well as *ab initio* methods such as multireference self-consistent-field (MC-SCF), have been carried out to identify the low-lying electronic and geometric features.[56−88] These studies generally give the following qualitative picture for long even polyenes:

(1) Excitations, coupled to lattice relaxation, break the dimerization of the ground state and lead to local geometrical defects.[89] For example, adiabatic relaxation gives rise to a central polaronic feature in the bright 1^1B_u state,[73,77,83,84] as well as two-soliton or four-soliton structures for the dark 2^1A_g state.[62,64,73]

(2) For short polyenes ranging from ethylene to octatriene, studies of low-lying excited state relaxation pathways

suggest that nonplanar molecular conformations are important at energy crossings.[90−106] This opens up the question of the nature of energy crossings and their associated geometries in the excited states of longer polyenes.

Here, using an *ab initio* Hamiltonian and DMRG-CI analytic energy gradients, we revisit these questions in the excited states of relatively long *trans*-polyacetylenes, with the objective of obtaining a more quantitative picture.

In sections 2 and 3, we start by reviewing analytic energy gradient theory and DMRG theory, respectively. In section 4, we discuss the formulation of DMRG analytic gradients. In section 5, we discuss the DMRG maximum overlap method for stable state-specific excited-state calculations without orthogonality constraints. In section 6, we apply our DMRG gradient algorithm to characterize the geometry and nature of the low-lying singlet states of the trans-polyenes.

2. GENERAL ENERGY GRADIENT THEORY FOR VARIATIONAL METHODS

For completeness, we briefly recall analytic energy gradient theory for variational wave functions. The energy referred to is the Born−Oppenheimer potential, which is the sum of the electronic energy and the nuclear−nuclear repulsion. The nuclear−nuclear repulsion gradient is trivial. The electronic energy $\langle \Psi | \hat{H} | \Psi \rangle$ is the expected value of the electronic Hamiltonian $\hat{H}$:

$$\hat{H} = \sum_{ij\sigma} t_{ij} c_{i\sigma}^\dagger c_{j\sigma} + \frac{1}{2} \sum_{ijkl\sigma\sigma'} v_{ijkl} c_{i\sigma}^\dagger c_{j\sigma'}^\dagger c_{k\sigma'} c_{l\sigma} \tag{1}$$

where i, j, k, and l are indices of orthogonal orbitals, and σ, $\sigma' = \{\uparrow, \downarrow\}$. $\hat{H}$ is dependent on the orbital functions through the integrals t_{ij} and v_{ijkl}. In a typical implementation, these orthogonal orbitals are represented as a linear combination of atomic orbitals (AOs) with orbital coefficients $\mathbf{C}$: $|i\rangle = \sum_\mu C_{i\mu} |\mu\rangle$, where we use Greek letters (μ, ν) to denote AO orbitals. The geometry dependence of the integrals arises from the AO functions, which (as Gaussian-type basis functions) is explicitly dependent on the nuclear positions, as well as through the LCAO coefficient matrix $\mathbf{C}$, which also changes with geometry. The Hamiltonian may be regarded as a function of the nuclear coordinates $\{a_i\}$ and the coefficient matrix $\mathbf{C}$: $\hat{H}(\{a_i\}, \mathbf{C})$. Since the electronic wave function $|\Psi\rangle$ is dependent on variational parameters $\{c_i\}$, the electronic energy is a function of $\{a_i\}$, $\mathbf{C}$, and $\{c_i\}$: $E(\{a_i\}, \mathbf{C}, \{c_i\})$. The energy gradient, with respect to nuclear coordinate a, takes the form

$$\frac{dE}{da} = \frac{\partial E}{\partial a} + \sum_{i\mu} \frac{\partial E}{\partial C_{i\mu}} \frac{dC_{i\mu}}{da} + \sum_i \frac{\partial E}{\partial c_i} \frac{dc_i}{da} \tag{2}$$

If $|\Psi\rangle$ is determined variationally, the energy is stationary to changes of $\{c_i\}$; thus, the third term vanishes. The gradient then is only dependent on the change in nuclear coordinates and orbital coefficients:

$$\frac{dE}{da} = \frac{\partial E}{\partial a} + \sum_{i\mu} \frac{\partial E}{\partial C_{i\mu}} \frac{dC_{i\mu}}{da} \tag{3}$$

It is convenient to rewrite the energy gradient in terms of density matrices. The energy is expressed as

$$E = \sum_{ij} t_{ij} \gamma_{ij} + \sum_{ijkl} v_{ijkl} \Gamma_{ijkl} \tag{4}$$

where $\gamma_{ij} = \sum_\sigma \langle \Psi | c_{i\sigma}^\dagger c_{j\sigma} | \Psi \rangle$ and $\Gamma_{ijkl} = \frac{1}{2} \sum_{\sigma\sigma'} \langle \Psi | c_{i\sigma}^\dagger c_{j\sigma'}^\dagger c_{k\sigma'} c_{l\sigma} | \Psi \rangle$ are the one- and two-particle density matrices. Since the second-quantized operators have no dependence on geometry, and the wave function is only dependent on $\{c_i\}$, it follows from eq 3 that the energy gradient is expressed in terms of the one- and two-electron derivative integrals and density matrices:

$$\frac{dE}{da} = \sum_{ij} \frac{dt_{ij}}{da} \gamma_{ij} + \sum_{ijkl} \frac{dv_{ijkl}}{da} \Gamma_{ijkl} \tag{5}$$

The one- and two-electron derivative integrals involve the orbital derivative (response), $d\mathbf{C}/da$. Writing

$$\frac{dC_{i\mu}}{da} = \sum_j U_{ij}^a C_{j\mu} \tag{6}$$

gives

$$\frac{dE}{da} = \sum_{ij} \frac{\partial h_{ij}}{\partial a} \gamma_{ij} + \sum_{ijkl} \frac{\partial v_{ijkl}}{\partial a} \Gamma_{ijkl} - \sum_{ij} X_{ij} \frac{\partial S_{ij}}{\partial a} + \sum_{ij} U_{ij}^a (X_{ij} - X_{ji}) \tag{7}$$

where $S_{ij} = \langle i | j \rangle$ is the overlap matrix of the orthogonal orbitals i and j,

$$S_{ij} = \sum_{\mu\nu} C_{i\mu} S_{\mu\nu} C_{j\nu} \tag{8}$$

and $S_{\mu\nu} = \langle \mu | \nu \rangle$ is the overlap matrix in the underlying AO basis. $\mathbf{X}$ is the Lagrangian matrix in the Generalized Brillouin Theorem (GBT),[107] which is given as

$$X_{ij} = \sum_m h_{im} \gamma_{mj} + 2 \sum_{mkl} v_{imkl} \Gamma_{jmkl} \tag{9}$$

characterizing the energy cost of electronic excitation from the *i*th orbital to the *j*th orbital. The gradient formula can be rewritten entirely in terms of AO quantities:[50]

$$\frac{dE}{da} = \sum_{\mu\nu} \gamma_{\mu\nu} \frac{dh_{\mu\nu}}{da} + \sum_{\mu\nu\rho\sigma} \Gamma_{\mu\nu\rho\sigma} \frac{dv_{\mu\nu\rho\sigma}}{da}$$
$$- 2 \sum_{\mu\nu} \sum_{i>j} \left(1 - \frac{\delta_{ij}}{2}\right) C_{i\mu} C_{j\nu} X_{ji} \frac{dS_{\mu\nu}}{da}$$
$$+ 2 \sum_{i\geq j} U_{ij}^a (X_{ij} - X_{ji}) \tag{10}$$

where $h_{\mu\nu}$, $\gamma_{\mu\nu}$, $v_{\mu\nu\rho\sigma}$, and $\Gamma_{\mu\nu\rho\sigma}$ are the one- and two-particle integrals and reduced density matrices, respectively, on the AO basis. Note that since the integrals are given on the AO basis, the total derivative and the partial derivative are the same; we use total derivatives when dealing with AO quantities.

Generally, the orbital derivative $dC_{i\mu}/da$ requires the solution of equations that couple the wave function coefficients c_i to the orbital coefficients $C_{i\mu}$. However, there are two common situations where the orbital response is simplified. The first is when the orbitals are defined independently of the correlated wave function, for example, for Hartree−Fock (HF) or Kohn−Sham (KS) orbitals. Using the Hartree−Fock canonical orbitals as an example, the orbital response $\mathbf{U}^a$ is defined by the Hartree−Fock convergence condition,

$$\frac{dF_{ij}}{da} = 0 \qquad (i \neq j) \tag{11}$$

which leads to the definition of the $\mathbf{U}^a$ matrix,

$$U_{ij}^a = \frac{1}{(\epsilon_j - \epsilon_i)}\left(\sum_k^{vir}\sum_l^{d.o.} A_{ij,kl}U_{kl}^a + B_{ij}^a\right) \tag{12}$$

where

$$A_{ij,kl} = 4v_{ijkl} - v_{ikjl} - v_{iljk}$$

$$B_{ij}^a = F_{ij}^a - S_{ij}^a\epsilon_j - \sum_{jk} S_{kl}^a(2v_{ijkl} - v_{ikjl}) \tag{13}$$

with $F_{ij}^a = \partial F_{ij}/\partial a$, $S_{ij}^a = \partial S_{ij}/\partial a$, and the various ϵ terms are HF orbital energies. Equation 12 is the coupled-perturbed Hartree−Fock (CPHF) equation,[108] and it uniquely defines the $\mathbf{U}^a$ matrix elements for canonical orbitals. In a similar way, other types of orbital response (for example, for the Kohn−Sham orbitals, or localized Hartree−Fock orbitals) can be computed from the corresponding coupled-perturbed single-particle equations.[49,109]

The second simplifying case is when the correlated wave function energy itself is stationary, with respect to orbital variations. In this case, $X_{ij} - X_{ji} = 0$, and the orbital response is not required, even though it is formally coupled to the correlated variational wave function coefficients. The energy gradient reduces to the simpler form

$$\frac{dE}{da} = \sum_{\mu\nu}\gamma_{\mu\nu}\frac{dh_{\mu\nu}}{da} + \sum_{\mu\nu\rho\sigma}\Gamma_{\mu\nu\rho\sigma}\frac{dv_{\mu\nu\rho\sigma}}{da}$$

$$- 2\sum_{\mu\nu}\sum_{i\geq j}\left(1 - \frac{\delta_{ij}}{2}\right)C_{i\mu}C_{j\nu}X_{ji}\frac{dS_{\mu\nu}}{da} \tag{14}$$

3. GENERAL DMRG THEORY

The DMRG is a variational wave function method.[110] For a set of L orthogonal orbitals (where the states for the ith orbital are $|\sigma_i\rangle = \{|0\rangle, |\uparrow\rangle, |\downarrow\rangle, |\uparrow\downarrow\rangle\}$), we choose a partitioning of the orbitals into a left block, single site, and right block, consisting of orbitals $\{1, ..., l - 1\}$, $\{l\}$, and $\{l+1, ..., L\}$, respectively. The corresponding canonical "one-site" DMRG wave function takes the matrix product form

$$|\Psi\rangle = \sum_{\sigma_1\sigma_2...\sigma_L}\mathbf{L}^{\sigma_1}\mathbf{L}^{\sigma_2}...\mathbf{L}^{\sigma_{l-1}} \times \mathbf{C}^{\sigma_l}\mathbf{R}^{\sigma_{l+1}}\mathbf{R}^{\sigma_{l+2}}...\mathbf{R}^{\sigma_L}|\sigma_1\sigma_2...\sigma_L\rangle \tag{15}$$

The (rotation) matrices $\mathbf{L}^{\sigma_i}$ and $\mathbf{R}^{\sigma_i}$ have dimensions of $M \times M$, except for the first and last, which have dimensions of $1 \times M$ and $M \times 1$, respectively. They satisfy the left- and right-canonical conditions

$$\sum_{\sigma_i}\mathbf{L}^{\sigma_i T}\mathbf{L}^{\sigma_i} = \mathbf{1}$$

$$\sum_{\sigma_i}\mathbf{R}^{\sigma_i}\mathbf{R}^{\sigma_i T} = \mathbf{1} \tag{16}$$

while the $\mathbf{C}^{\sigma_l}$ (wave function) matrix satisfies the normalization condition

$$\text{tr}\sum_{\sigma_l}\mathbf{C}^{\sigma_l T}\mathbf{C}^{\sigma_l} = 1 \tag{17}$$

Together, $\{\mathbf{L}^{\sigma_i}\}$, $\{\mathbf{C}^{\sigma_i}\}$, and $\{\mathbf{R}^{\sigma_i}\}$ contain the variational parameters. As in other variational methods, the coefficients of the matrices are determined by minimizing the energy. In principle, a direct gradient minimization of the energy, with respect to all the matrices, subject to the canonical conditions (eqs 16 and 17) may be performed. In practice, the DMRG sweep algorithm is normally used. Here, at a given step l of the sweep, corresponding to the block partitioning $\{1, ..., l-1\}$, $\{l\}$, and $\{l+1, ..., L\}$, the energy is minimized only with respect to the $\mathbf{C}^{\sigma_l}$ wave function matrix, with the $\{\mathbf{L}^{\sigma_i}\}$, $\{\mathbf{R}^{\sigma_i}\}$ rotation matrices being held fixed. The minimizing $\mathbf{C}^{\sigma_l}$ is obtained from an effective ground-state eigenvalue problem

$$\mathbf{Hc} = E\mathbf{c} \tag{18}$$

where c denotes $\mathbf{C}^{\sigma_l}$ flattened into a single vector, and $\mathbf{H}$ denotes $\hat{H}$ expressed in the basis of renormalized basis states defined by the $\{\mathbf{L}^{\sigma_i}\}$ and $\{\mathbf{R}^{\sigma_i}\}$ matrices.[110] In the next step of the sweep, the single site is moved from l to $l+1$ (or from l to $l-1$ in a backward sweep). To satisfy the new canonical form with the single site at $l+1$, where the $\mathbf{C}^{\sigma_l}$ matrix is replaced by an $\mathbf{L}^{\sigma_l}$ matrix, and the $l+1$ site is associated with a new $\mathbf{C}^{\sigma_{l+1}}$ matrix, we use the gauge relations,

$$\mathbf{C}^{\sigma_l} = \mathbf{L}^{\sigma_l}\Lambda$$

$$\mathbf{C}^{\sigma_{l+1}} = \Lambda\mathbf{R}^{\sigma_{l+1}} \tag{19}$$

By sweeping through all the partitions $l = 1, ..., L$, and minimizing with respect to the $\mathbf{C}^{\sigma_l}$ matrix at each partition, the DMRG sweep algorithm ensures that all the variational degrees of freedom in the DMRG wave function are optimized.

An important aspect of DMRG calculations is the enforcement of symmetries, including global symmetries such as the total particle number and spin. In the DMRG wave function, Abelian global symmetries (such as total particle number) are enforced by local quantum numbers. For example, to enforce a total particle number of N in the wave function, each value of the three indices σ, i, and j in the matrix elements $\mathbf{L}_{ij}^\sigma$, $\mathbf{R}_{ij}^\sigma$, and $\mathbf{C}_{ij}^\sigma$ can be associated with an additional integer N_i, N_j, and N_σ. (These values can be interpreted in terms of the particle numbers of the renormalized states (for N_i and N_j) and for the states of the single site (for N_σ).) A total particle number of N then is enforced, with the following rules:

$$\mathbf{L}: \qquad N_i + N_\sigma = N_j$$

$$\mathbf{R}: \qquad N_j + N_\sigma = N_i$$

$$\mathbf{C}: \qquad N_i + N_\sigma + N_j = N \tag{20}$$

Applying these conditions to $\mathbf{L}_{ij}^\sigma$, $\mathbf{R}_{ij}^\sigma$, and $\mathbf{C}_{ij}^\sigma$ means that the matrices have a block-sparse structure, which is important to maintain during geometry optimization.

4. STATE-SPECIFIC DMRG ANALYTIC ENERGY GRADIENTS

At convergence of the above (one-site) DMRG sweep algorithm, the contribution of the wave function coefficients to the gradient (dc_i/da in eq 2) vanishes, as expected for a variational wave function method. Thus, the analytic energy gradient theory for variational wave functions described in section 2 can be applied.

We will consider energy gradients for two types of DMRG calculations. The first are DMRG configuration interaction (DMRG-CI) analytic gradients, using HF canonical orbitals. In this case, the orbital response is given by the CPHF equations,

presented in section 2. The DMRG calculations are carried out within an active space, chosen as a subset of the canonical orbitals. Because the DMRG wave function is not invariant to rotations of the active space orbitals for small M, the contribution of the active orbital response must be computed, specifying a particular orbital choice (rather than just their manifold), such as the canonical HF orbitals.

The algorithm to compute the DMRG-CI analytic gradient with HF canonical orbitals is as follows:

(1) Solve the HF equations for the canonical orbital coefficient matrix $\mathbf{C}$.

(2) Select an active space and solve for the DMRG wave function in this space. Compute the one- and two-particle reduced density matrices γ_{ij} and Γ_{ijkl} at the convergence of the single-site sweep algorithm.

(3) Compute the AO derivative integrals $dh_{\mu\nu}/da$, $dv_{\mu\nu\rho\sigma}/da$, and $dS_{\mu\nu}/da$, and the matrix $\mathbf{X}$ in eq 9.

(4) Use the derivative integrals to construct the CPHF equation in eq 12 (or the equivalent Z-vector equation[50]) and solve for $\mathbf{U}^a$ for all nuclear coordinates.

(5) Compute the energy gradient by contractions of all of the above integrals and matrices, according to eq 7 or eq 10.

The second type of DMRG calculation that we consider is a DMRG complete active space self-consistent field (DMRG-CASSCF) calculation. For DMRG-CASSCF wave functions, the DMRG energy is stationary to any orbital rotation; thus,

$$X_{ij} - X_{ji} = 0 \tag{21}$$

and, using eqs 7 and 10, this means that the orbital response is not required, even though it is coupled to the response of the DMRG wave function. However, because the DMRG wave function is not invariant to active space rotations for small M, it is necessary to optimize the active–active rotations also, unlike in a traditional CASSCF calculation. Alternatively, if active–active rotations are omitted, the DMRG-CASSCF gradient can be viewed as an approximate gradient with a controllable error from active–active contributions (which vanishes as M is extrapolated to ∞).

The algorithm for the DMRG-CASSCF gradient is described as follows:

(1) Solve for the DMRG-CASSCF orbitals with the one-site DMRG wave function. In each macroiteration:

  (a) Solve for the one-site state-specific DMRG wave function and compute the one- and two-body reduced density matrices γ_{ij} and Γ_{ijkl}.

  (b) Using γ_{ij} and Γ_{ijkl}, compute the orbital gradient and Hessian, both of which include elements for active–active rotations.

  (c) Update the orbitals with the orbital rotation matrix.

(2) Compute the AO density matrices $\gamma_{\mu\nu}$ and $\Gamma_{\mu\nu\rho\sigma}$ at the convergence of DMRG-CASSCF.

(3) Compute the AO derivative integrals $dh_{\mu\nu}/da$, $dv_{\mu\nu\rho\sigma}/da$ and $dS_{\mu\nu}/da$.

(4) Contract all the above integrals and matrices using eq 14 to obtain the energy gradients.

5. ADIABATIC ORBITAL AND WAVE-FUNCTION PROPAGATION AND EXCITED-STATE TRACKING

Geometry optimization requires adiabatic propagation along a potential energy surface. For a DMRG calculation, this means that, in each geometry step, the orbitals defining the active space should change continuously, and the quantum numbers and associated block-sparsity pattern of the matrices should not change. The former can be achieved using maximum overlap techniques, while the latter can be done by fixing the quantum numbers at the initial geometry. For state-specific excited-state calculations, the maximum overlap technique is further important to prevent root flipping. Root flipping in state-specific DMRG calculations arises because the matrices optimized in the wave function for one state (eq 15) are not optimal for another state.[111] (Note that the gradient formalism presented above is only valid for state-specific, rather than state-averaged, DMRG calculations.)

5.1. Orbital Maximum Overlap. The maximum overlap technique for the orbitals involves computing the overlap matrix between molecular orbitals (MOs) of the $(m-1)$th and mth step:

$$
\begin{aligned}
S_{ij}^{m-1,m} &= \langle \psi_i^{m-1} | \psi_j^m \rangle \\
&= \sum_{\mu\nu} C_{i\mu}^{m-1} C_{j\nu}^m \langle \phi_\mu^{m-1} | \phi_\nu^m \rangle
\end{aligned}
\tag{22}
$$

where $\langle \phi_\mu^{m-1} | \phi_\nu^m \rangle$ are the AO overlap matrix elements of the $(m-1)$th and mth steps. For the active space, we choose the orbitals at step m with maximum overlap with the active space orbitals at step $(m-1)$. Equation 22 also allows us to align the MO phases for adjacent geometry optimization steps.

5.2. Excited-State Tracking in DMRG. We further use maximum overlap of the DMRG wave functions to target and track the correct state-specific excited state solution. Within the standard ground-state sweep algorithm at a given geometry, the desired excited state can usually be found in the eigenspectrum at the middle of the sweep (when the renormalized Hilbert space is largest) but can be lost at the edges of the sweep when the renormalized Hilbert space is small (if it is generated for the incorrect eigenvector). To keep following the excited state across the sweep by generating the appropriate renormalized Hilbert space, we ensure that, at each block iteration, we always pick the Davidson solution with maximum overlap with the excited state solution at the previous block iteration. Between geometries, we ensure that we are tracking the correct excited state by computing the overlap between the DMRG wave functions at the different geometries. In principle, this requires multiplying the overlaps between the $\mathbf{L}^\sigma$ and $\mathbf{R}^\sigma$ matrices, and $\mathbf{c}$ vectors. However, we find it is sufficient (and, of course, less expensive) to compute only the overlap between the $\mathbf{c}$-vectors for the two geometries, at the middle of the sweeps.

The state-specific DMRG wave function maximum overlap scheme is described as follows:

(1) At the initial geometry, use a state-averaged DMRG algorithm to obtain initial guesses for n states.[111] (The more-robust two-site DMRG algorithm may be used here,[112] and a highly accurate initial guess for a small M can be obtained by running back sweeps from large M.[113]) Store the wave function vectors $\{\mathbf{c}^i\}$ (for $i = 1, 2, ..., n$) at the middle of the sweep. Note that, in the state-averaged procedure, all n states share the same left and right rotation matrices $\{\mathbf{L}^\sigma\}$ and $\{\mathbf{R}^\sigma\}$.

(2) At a new geometry optimization step (equal to the initial geometry in the first step), restart the DMRG sweep with the same M from the previous solution for the targeted excited state, and use state-specific DMRG with the *one-site* sweep algorithm to get the new solution for the targeted excited state. (Note that any noise in the DMRG algorithm should be turned

off.) At each block iteration, apply the following steps in the Davidson solver:

(a) Perform DMRG wave function prediction by eq 19 from the previous block iteration, to obtain guess vectors $\{c_{guess}^i\}$ for the current block iteration.

(b) Perform the Block−Davidson algorithm to obtain solutions $\{c_{sol}^i\}$.

(c) Compute overlaps between vectors $\{c_{sol}^i\}$ and $\{c_{guess}^i\}$, and align the phases when needed.

(d) Choose the new solution c_{sol}^x in $\{c_{sol}^i\}$ for the targeted excited state, from the largest overlap between c_{sol}^x and c_{guess}^n.

(e) Store the vector c_{sol}^x as the new solution.

(3) Repeat step 2 in further geometry optimization steps.

6. EXCITED-STATE GEOMETRIES OF TRANS-POLYENES

Excited-state geometry optimization in linear polyenes serves as a starting point to understand the photophysical and photochemical behavior of analogous systems, such as the carotenoids, in biological processes. We take, as our systems, the *trans*-polyacetylenes $C_{2n}H_{2n+2}$, with $n = 5-10$. We modeled the excited states and geometry relaxation as follows:

(1) We obtained ground-state S_0 (1^1A_g) geometries with DFT/B3LYP.[114]

(2) We then used the DFT ground-state geometries as initial guesses to perform ground-state geometry optimization with DMRG-CI analytic energy gradients.

(3) We recomputed excited states at the DMRG optimized ground-state geometries.

(4) We then further relaxed the excited-state geometries with the DMRG-CI gradients. All calculations were performed with the cc-pVDZ basis set.[115−117]

The active spaces were chosen as (n_e, n_o), where n is the total number of π electrons. We identified the π active spaces consisting of C $2p_z$ orbitals from the Löwdin MO population analysis at the initial geometry, and tracked the active spaces through the geometry relaxation with the orbital maximum overlap method in section 5.1. We also carried out additional calculations with a second "energy-ordered" active space, consisting of the lowest π and σ orbitals to comprise an (n_e, n_o) active space. We clearly distinguish when we are referring to the second active space in the discussion below. The initial ground-state DFT/B3LYP geometry optimizations were carried out with the MOLPRO quantum chemistry package.[118] State-specific DMRG wave functions were obtained with the BLOCK DMRG program,[3,8,21,119] using the state-specific and adiabatic wave function tracking by wave function maximum overlap in section 5.2. DMRG-CI gradients were implemented in the ORCA quantum chemistry package.[120] All calculations worked in the canonical HF orbital basis (no localization). To improve the geometry optimization, we employed approximate nuclear Hessians, updated by the BFGS method.[121−124]

To simplify the analysis, in this work, we only considered geometry optimization *in the plane*. Nonplanar geometries are of course relevant to polyene excited states but even at planar geometries, important features of the electronic excited-state geometries (e.g., the solitonic structure) appear and remain to be understood at an *ab initio* level. The planar optimization was not enforced explicitly other than through a planar initial guess, and otherwise the coordinates were allowed to relax in all

degrees of freedom. Consequently, electronic wave functions were computed within C_1 spatial point group symmetry. We used three different numbers of renormalized states M = 100, 500, 1000 to obtain DMRG wave functions for all states, to examine the influence of wave function accuracy on the geometries. Converging DMRG wave functions to a high accuracy ensures the accuracy of the particle density matrices, which then ensures that the correct geometric minima can be reached. However, when the magnitude of gradients was much larger than the unconverged DMRG error, (for example, when the geometry was far from the equilibrium) loose DMRG convergence and fewer sweeps were used to decrease the computational time.

To further characterize the low-lying excited states, we analyzed the exciton and bimagnon character of state transitions using the transition particle density matrices. The first-order transition density matrix element in the MO basis between the ground (GS) and excited states (ES) is

$$\langle \Psi_{ES} | c_i^\dagger c_j | \Psi_{GS} \rangle \tag{23}$$

where i and j denote spatial MO indices. We used the first-order transition density matrix to locate the first optically dark and bright states by the following well-established state signatures:

(1) A single large element, where i = LUMO, j = HOMO, indicating the first optically bright state; and

(2) Two dominant elements, where i = (LUMO+1), j = HOMO, and i = LUMO, j = (HOMO−1), indicating the first optically dark state.

Real-space particle−hole excitation patterns were further analyzed by the real-space first-order transition density matrix, which was obtained by transforming the vir−occ block of the MO first-order transition density matrix to the orthogonal $2p_z$ basis. Real-space particle-hole excitation patterns were characterized by excitations of an electron from an orbital at $R - r/2$ to an orbital to $R + r/2$, where R was set at the center of a polyene chain, and r is the particle−hole separation length. We illustrate the excitons graphically by plotting $\langle c_p^\dagger c_{n-p} \rangle$, where p is the index of the C $2p_z$ orbital, and n is the total number of $2p_z$ orbitals in the chain.

Similarly, the real-space bimagnon character is characterized by the real-space double-spin flip transition density

$$\langle \Psi_{ES} | c_{p,\sigma}^\dagger c_{p,-\sigma} c_{n-p,-\sigma}^\dagger c_{n-p,\sigma} | \Psi_{GS} \rangle \tag{24}$$

where $\sigma = \{\uparrow, \downarrow\}$. The real-space second-order transition density matrix was transformed from the vir−vir−occ−occ block of the MO basis second-order transition density matrix.

Analogously to previous studies, we further examined bond orders and geometrical defects (solitons) through the bond length alternation (BLA) function δ_n:

$$\delta_n = (-1)^{n+1}(x_{n+1} - x_n) \tag{25}$$

where $n = 1, ..., N_{bond}$ and x denotes bond lengths. For even-site *trans*-polyacetylenes, the two edge bonds at the ground state are always double bonds, thus δ_n will always be positive. Consequently, negative values of δ_n indicate a reversed bond order, and a vanishing ($\delta_n = 0$) value comes from two equal bond lengths, i.e., an undimerized region.

6.1. State Signatures and Geometries. *6.1.1. Ground State S_0.* The ground state of polyenes is denoted by the symmetry label 1^1A_g (here, we are using symmetry labels

characteristic of idealized C_{2h} symmetry) and the relaxed ground-state geometries are planar and dimerized. For the ground state, DMRG wave functions with $M = 100$ are sufficient to achieve qualitative accuracy in bond lengths of our studied polyenes. $M = 500$ is sufficient for quantitative accuracy. For example, $M = 100$ produced errors of no more than 0.0067 Å for $C_{20}H_{22}$, while $M = 500$ converged the bond lengths to an error of 0.0013 Å, compared to bond lengths using $M = 1000$ (near exact). This finding is consistent with the ground-state wave function of even-carbon trans-polyenes being mostly a single determinant, and thus accurately described by DMRG in the canonical molecular orbital basis with small M.

The BLA function δ_n of the relaxed ground-state geometry of $C_{20}H_{22}$ from DMRG and DFT is shown in Figure 1. The BLA
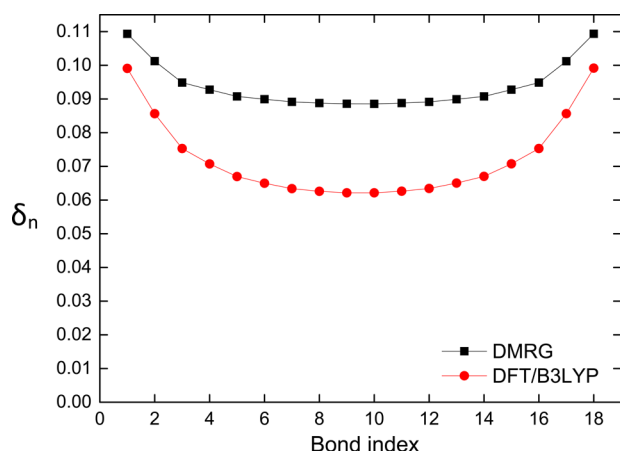

Figure 1. Bond length alternation function δ_n for relaxed ground-state geometries of $C_{20}H_{22}$, from left to right.

functions from both DMRG and DFT give the same pattern, showing a weaker dimerization in the middle region, compared to the edges of the carbon chain. Compared to the dimerization in DFT, the dimerization in the DMRG calculations is increased, indicating a larger dimerization gap.

6.1.2. Excited States. The first optically bright state in the single-π complete active space is the *third* excited state S_3, and is denoted by the symmetry label 2^1B_u. The corresponding MO based first-order transition density matrix between S_3 and S_0 (defined by eq 23) possesses an element ~ 1.0, where $i =$ LUMO and $j =$ HOMO, along with other elements ≤ 0.1. This signals a (HOMO $\rightarrow$ LUMO) single particle–hole transition, characteristic of the first optical transition.

The 1^1B_u state corresponds to the second excited state S_2 in the single-π active space. Notable first-order excitations in the S_0/S_2 transition (for instance, in $C_{10}H_{12}$) are (HOMO $\rightarrow$ LUMO+2) and (HOMO−2 $\rightarrow$ LUMO) excitations, both with elements ~ 0.5 at the ground-state equilibrium geometry. A large (HOMO $\rightarrow$ LUMO) excitation is missing for the S_0/S_2 transition for all the polyenes, ruling it out as the usual bright state. Note that the order of excited states is dependent on the choice of active space (i.e., the effective Hamiltonian). If one changes from the single-π active space to an energy-ordered active space, which includes both σ and π orbitals within the (n_e, n_o) active space window, one finds that the 1^1B_u state is an S_2 state corresponding to the physical optically bright HOMO $\rightarrow$ LUMO transition. These excitation energies are reported in the Supporting Information. This demonstrates the

well-known strong effect of dynamical correlation on the low-lying excited state order in linear polyenes.

The first optically dark state is the S_1 state, denoted by 2^1A_g. The S_0/S_1 transition exhibits dominant (HOMO $\rightarrow$ LUMO+1) and (HOMO−1 $\rightarrow$ LUMO) single excitations, along with a dominant (HOMO, HOMO $\rightarrow$ LUMO, LUMO) double excitation. The position of this low-lying excited state remains as the S_1 state in an energy-ordered active space.

For the bright state, optimized bond lengths were not strongly dependent on M. For a small system such as $C_{10}H_{12}$, $M = 100$ produced a largest error of 0.0018 Å in the bond lengths, compared to the $M = 1000$ result. For a larger system, such as $C_{20}H_{22}$, the bond lengths at $M = 100$ differed from those at $M = 1000$ by no more than 0.0059 Å, and the largest error at $M = 500$ was only 0.0009 Å. For the dark state, however, the precision of the optimized geometry was more sensitive to the choice of M for the longer polyenes. This may not be surprising, as the first optically bright state is mainly a single-reference state, while the lower dark state has more challenging multireference character.[125] For all the polyenes considered, if we use small M, the largest error in the bond lengths of the dark state occurs for bonds around the geometrical defects (solitons). In $C_{20}H_{22}$, the largest error at $M = 100$ is ~ 0.025 Å, coming from the bonds C_3−C_4 and C_{17}−C_{18} which are around the solitons (see section 6.3). On the other hand, central bonds in the dark state are much less dependent on M, e.g., $M = 100$ yields errors of ≤ 0.012 Å for bonds from C_7−C_8 to C_{13}−C_{14} in $C_{20}H_{22}$. In a localized real-space view, this behavior reflects the strong localization of multireference electronic structure around the geometrical defects.

6.2. Excitation Energy. We show vertical and relaxed excitation energies as a function of $1/n$ for the first optically dark (2^1A_g) and first optically bright (2^1B_u) states for all considered $C_{2n}H_{2n+2}$ in Figure 2. Compared to the experimental
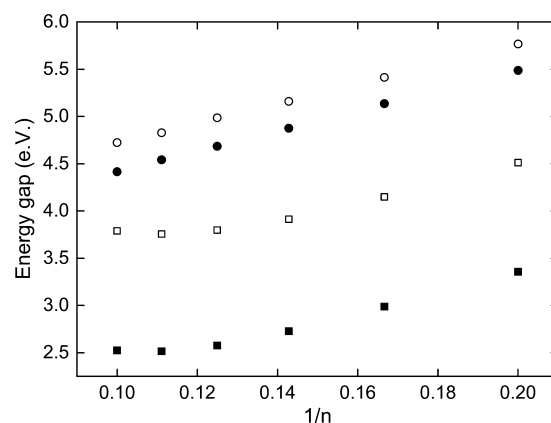

Figure 2. Vertical and relaxed excitation energies from DMRG optimized geometries: vertical S_0−S_1 (opened squares), vertical S_0−S_3 (opened circles), relaxed S_0−S_1 (solid squares), and relaxed S_0−S_3 (solid circles).

excitation energies for $C_{10}H_{12}$ to $C_{14}H_{16}$ in hydrocarbon solutions,[126] our relaxed excitation energies are 0.3 eV higher for the relaxed dark state, and 1.8 eV higher for the bright state. This is partially due to the lack of dynamic correlation in our calculations, as well as basis and solvent effects.

The dark state is always observed as below the bright state. We observe relaxation energies for all the polyenes of ~ 0.29 eV

for the bright state and ~1.20 eV for the dark state. The substantial relaxation energy for the dark state is consistent with the much larger geometry relaxation, compared to the bright state.[75]

Our calculations find that the 1^1B_u state lies relatively close to the 2^1B_u state at the ground-state equilibrium geometry, with a $1^1B_u - 2^1B_u$ energy gap (0.17–0.48 eV) for all the polyenes. Given the small magnitude of this energy gap, it seems likely that there can be an energy crossing between 2^1B_u and 1^1B_u states. If we use the energy-ordered active space, we do find an energy crossing between these states for $C_{20}H_{22}$ at a planar geometry, near the Franck–Condon region (see Figure 3). Of course, we also expect nonplanar conical intersections, as previously found in butadiene[104,105] and octatriene.[106]
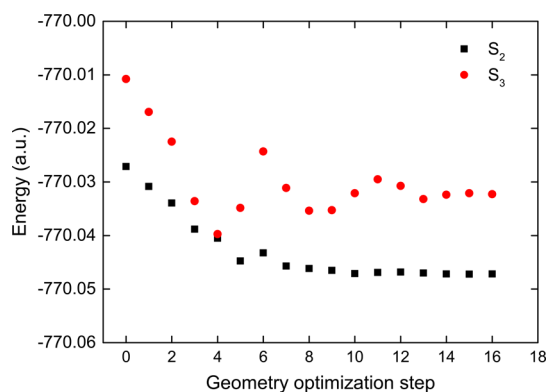

Figure 3. Energies of the S_2 and S_3 states in the S_2 geometry optimization of $C_{20}H_{22}$, computed with the energy-ordered active space, as a function of the geometry relaxation step. At the ground-state equilibrium (step 0), the S_2 and S_3 states are 1^1B_u (first bright state) and 2^1B_u states, respectively. At step 4, the molecule gives an S_2 and S_3 gap of 0.019 eV, which is strongly indicative of a conical intersection. After this step, the 1^1B_u and 2^1B_u states are swapped in terms of the state energy order. (Note that the S_3 state energy oscillates as only the S_2 state energy is being minimized.) The molecular geometry remains planar along the relaxation.

6.3. Solitons. The BLA δ_n functions for the first optically dark (2^1A_g) and first optically bright (2^1B_u) states are shown in Figures 4 and 5, respectively. These curves are almost parallel across all the polyenes for the dark and bright state, indicating generally similar behavior across the systems.
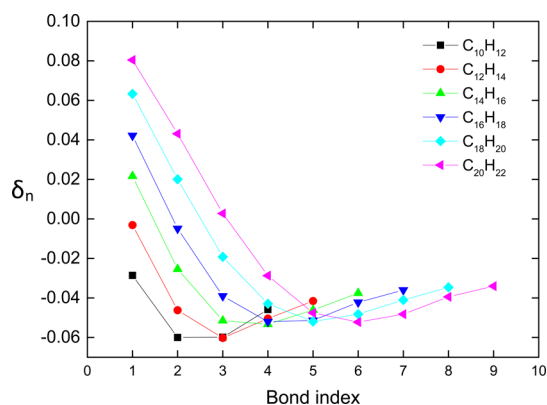

Figure 4. Bond length alternation function δ_n for relaxed first dark state geometries, from edge (left) to center (right).
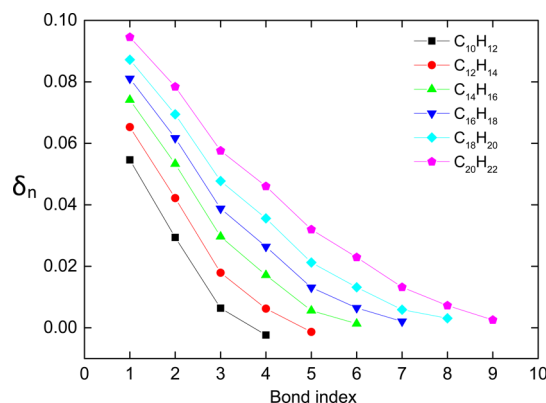

Figure 5. Bond length alternation function δ_n for relaxed first bright state geometries, from edge (left) to center (right).

For the 2^1A_g state, the BLA in short polyenes $C_{10}H_{12}$ and $C_{12}H_{14}$ is completely reversed from the ground state, as shown by the all negative δ_n values along the chain. The reversal of BLA in 2^1A_g in short polyenes has previously been understood in terms of the dominant valence bond configurations[66] with reversed BLA. For long polyenes, undimerization emerges near the edges, as shown by changes in the sign of the δ_n functions, and the BLA is opposite on the two sides of the undimerized regions. This result is in agreement with earlier semiempirical studies on long polyenes,[74,75] and our result shows the two-soliton structure in the relaxed 2^1A_g state.

For the 2^1B_u relaxed geometry, δ_n systematically shows a polaronic defect in the chain center. This is also consistent with previous semiempirical studies.[74,75] For short polyenes, the vanishing dimerization in the central region can be understood in terms of ionic valence band (VB) configurations along the chain.[66] In terms of excitons, the polaronic geometry is also viewed as evidence of a bound particle–hole excitation localized near the chain center.[89]

6.4. Excitons. Within the one-electron manifold, we can visualize the excitons with the real space particle–hole excitation density $\langle c_p^\dagger c_{n-p} \rangle$. As we relax the geometry, we can observe the shape of the exciton change. Geometry relaxation is important to overcome the exciton self-trapping,[89] e.g., in a polyene chain in its dimerized ground-state geometry. The real-space particle–hole excitation densities of $C_{20}H_{22}$ are shown in Figures 6 and 7, for the bright and dark states, respectively.

At the ground-state equilibrium geometry (i.e., a dimerized geometry), the particle–hole excitations of the bright state are strongly bound, as seen in Figure 6a. This is similar to that observed in the single-peak real-space exciton structure from DFT-GWA-BSE calculations,[127] as well as the $n = 1$ Mott–Wannier exciton pattern in the weak-coupling limit.[74] For the dark state, particle–hole pairs are slightly separated at the dimerized geometry, as illustrated by the double-peak real-space exciton structure in Figure 7a. This has been identified in previous studies,[74,127] as an $n = 2$ Mott–Wannier exciton. However, the amplitudes of the densities are 10 times smaller, compared to that of the bright state, essentially suggesting negligible exciton character for the dark state reached by a vertical transition.

After geometry relaxation, the particle–hole separation in the bright state increases, although the particle–hole pair remains bound at the bright state equilibrium geometry, as shown in Figure 6b. For the dark state, however, geometry relaxation seems to unbind the particle–hole pair, as shown by largely
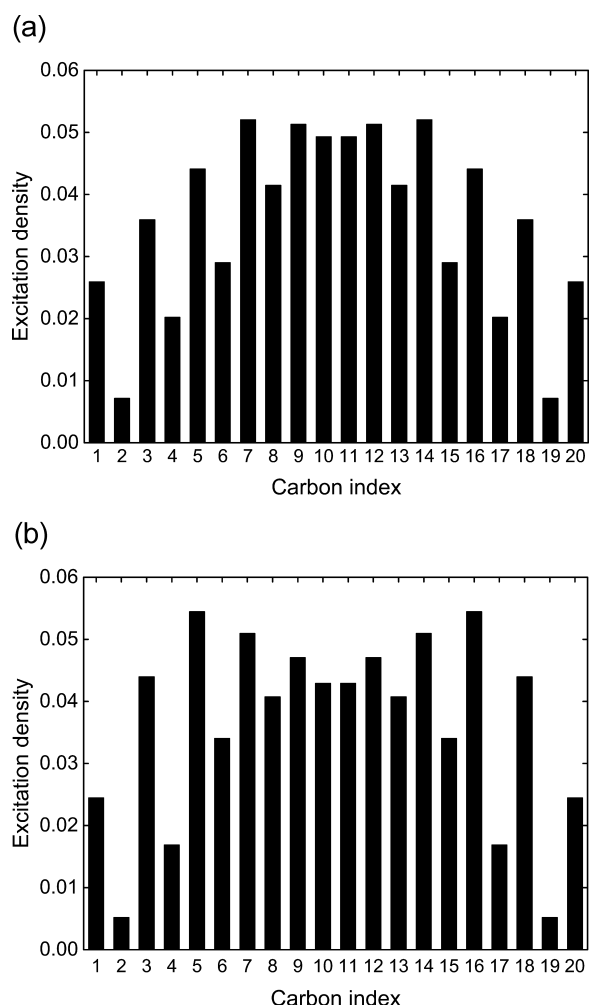
(a)

(b)

Figure 6. Real-space particle−hole excitation density of $C_{20}H_{22}$ between the ground state and the first bright state, computed at relaxed geometries of (a) the ground state (b) the first bright state.

separated peaks in Figure 7b. Along with the enhanced transition density amplitude, this suggests the emergence of a long-distance charge-transfer character associated with the dark state equilibrium geometry.

6.5. Bimagnons and Singlet Fission in 2^1A_g. The relaxed dark state 2^1A_g geometry possesses a separate two-soliton structure, as discussed in section 6.3. The locally undimerized regions in the relaxed 2^1A_g state can be thought to arise from a form of "internal singlet fission",[89] i.e., forming local triplets (magnons) while the total spin remains a singlet. The local triplets can be identifed from the local peaks of the real-space spin−spin correlation function of the 2^1A_g wave function, as in ref 74.

Here, we can also characterize the bimagnon character by the real-space double-spin flip transition density between the S_0 and 2^1A_g states (see eq 24). We show the real-space double-spin flip transition density of $C_{20}H_{22}$, as a function of the site index, in Figure 8. At the ground-state equilibrium, the bimagnons are confined near the chain center, as indicated by the local central double peaks. However, the bimagnons are highly mobile, and with geometry relaxation, the singlet fission character becomes much more delocalized. The transition density distribution possesses two peaks at C3 and C18 at the dark state
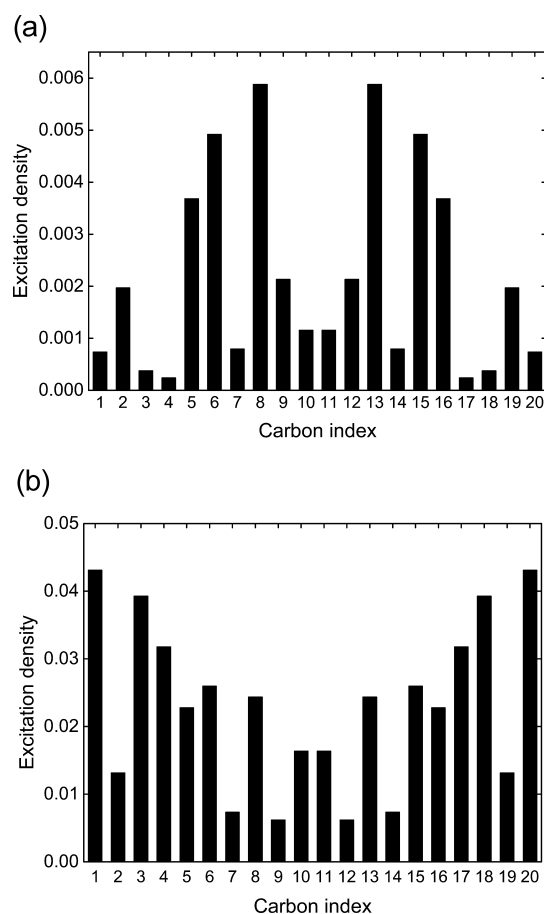
(a)

(b)

Figure 7. Real-space particle−hole excitation density of $C_{20}H_{22}$ between the ground state and the first dark state, computed at relaxed geometries of (a) the ground state (b) the first dark state.
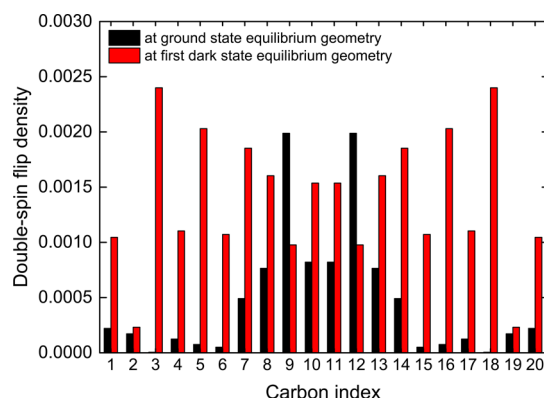

Figure 8. Real-space double-spin flip density between the ground state and the first dark state.

equilibrium geometry, which is consistent with the positions of the solitons shown in Figure 4.

7. CONCLUSIONS

We have presented a detailed formalism for state-specific analytic density matrix renormalization group (DMRG) energy gradients, including a maximum overlap algorithm that facilitates state-specific excited-state geometry optimizations. We employed these techniques to study the ground- and excited-state electronic and geometric structure of the polyenes at the level of DMRG configuration interaction (DMRG-CI).

Our quantitative results are consistent with earlier qualitative semiempirical studies of the exciton, bimagnon, and soliton character of the excited states. In addition to complex bond-length alternation patterns, we find evidence for a planar conical intersection.

DMRG analytic energy gradients provide a path toward the dynamical modeling of excited-state and highly correlated quantum chemistry. The interaction of dynamic and non-adiabatic effects with strong electron correlation remains an open issue, which can now be explored with the further development of the techniques described here.

■ ASSOCIATED CONTENT

Ⓢ Supporting Information

Excitation energies, optimized bond lengths, and relaxed geometries calculated with DMRG-CI analytic energy gradients. This material is available free of charge via the Internet at The Supporting Information is available free of charge on the ACS Publications website at DOI: 10.1021/acs.jctc.5b00174.

■ AUTHOR INFORMATION

Corresponding Author
*E-mail: gkchan@princeton.edu.
Notes
The authors declare no competing financial interest.

■ ACKNOWLEDGMENTS

■ REFERENCES

(1) White, S. R.; Martin, R. L. *J. Chem. Phys.* **1999**, *110*, 4127−4130.
(2) Mitrushenkov, A. O.; Fano, G.; Ortolani, F.; Linguerri, R.; Palmieri, P. *J. Chem. Phys.* **2001**, *115*, 6815.
(3) Chan, G. K.-L.; Head-Gordon, M. *J. Chem. Phys.* **2002**, *116*, 4462−4476.
(4) Legeza, Ö.; Röder, J.; Hess, B. *Phys. Rev. B* **2003**, *67*, 125114.
(5) Legeza, Ö.; Röder, J.; Hess, B. *Mol. Phys.* **2003**, *101*, 2019−2028.
(6) Legeza, Ö.; Sólyom, J. *Phys. Rev. B* **2003**, *68*, 195116.
(7) Legeza, Ö.; Sólyom, J. *Phys. Rev. B* **2004**, *70*, 205118.
(8) Chan, G. K.-L. *J. Chem. Phys.* **2004**, *120*, 3172−3178.
(9) Moritz, G.; Hess, B. A.; Reiher, M. *J. Chem. Phys.* **2005**, *122*, 024107.
(10) Moritz, G.; Wolf, A.; Reiher, M. *J. Chem. Phys.* **2005**, *123*, 184105.
(11) Rissler, J.; Noack, R. M.; White, S. R. *Chem. Phys.* **2006**, *323*, 519−531.
(12) Legeza, Ö., Noack, R., Sólyom, J., Tincani, L. *Computational Many-Particle Physics*; Fehske, H., Schneider, R., Weiße, A., Eds.; Springer: Berlin, New York, 2008; pp 653−664.
(13) Chan, G. K.-L.; Zgid, D. *Ann. Rep. Comput. Chem.* **2009**, *5*, 149−162.
(14) Marti, K. H.; Reiher, M. *Z. Phys. Chem.* **2010**, *224*, 583−599.
(15) Chan, G. K.-L.; Sharma, S. *Annu. Rev. Phys. Chem.* **2011**, *62*, 465−481.
(16) Zgid, D.; Nooijen, M. *J. Chem. Phys.* **2008**, *128*, 144116.
(17) Zgid, D.; Nooijen, M. *J. Chem. Phys.* **2008**, *128*, 144115.
(18) Ghosh, D.; Hachmann, J.; Yanai, T.; Chan, G. K.-L. *J. Chem. Phys.* **2008**, *128*, 144117.
(19) Luo, H.-G.; Qin, M.-P.; Xiang, T. *Phys. Rev. B* **2010**, *81*, 235129.
(20) Zgid, D.; Nooijen, M. *J. Chem. Phys.* **2008**, *128*, 014107.
(21) Sharma, S.; Chan, G. K.-L. *J. Chem. Phys.* **2012**, *136*, 124121.
(22) Wouters, S.; Poelmans, W.; Ayers, P. W.; van Neck, D. *Comput. Phys. Commun.* **2014**, *185*, 1501−1514.
(23) Neuscamman, E.; Yanai, T.; Chan, G. K.-L. *J. Chem. Phys.* **2010**, *132*, 024106.
(24) Yanai, T.; Kurashige, Y.; Neuscamman, E.; Chan, G. K.-L. *J. Chem. Phys.* **2010**, *132*, 024105.
(25) Kurashige, Y.; Yanai, T. *J. Chem. Phys.* **2011**, *135*, 094104.
(26) Dorando, J. J.; Hachmann, J.; Chan, G. K.-L. *J. Chem. Phys.* **2009**, *130*, 184111.
(27) Nakatani, N.; Wouters, S.; Van Neck, D.; Chan, G. K.-L. *J. Chem. Phys.* **2014**, *140*, 024108.
(28) Chan, G. K.-L.; Head-Gordon, M. *J. Chem. Phys.* **2003**, *118*, 8551−8554.
(29) Chan, G. K.-L.; Kállay, M.; Gauss, J. *J. Chem. Phys.* **2004**, *121*, 6110−6116.
(30) Sharma, S. arXiv preprint arXiv:1408.5868 2014.
(31) Sharma, S.; Yanai, T.; Booth, G. H.; Umrigar, C. J.; Chan, G. K.-L. *J. Chem. Phys.* **2014**, *140*, 104112.
(32) Chan, G. K.-L.; Van Voorhis, T. *J. Chem. Phys.* **2005**, *122*, 204101.
(33) Hachmann, J.; Cardoen, W.; Chan, G. K.-L. *J. Chem. Phys.* **2006**, *125*, 144101.
(34) Hachmann, J.; Dorando, J. J.; Avilés, M.; Chan, G. K.-L. *J. Chem. Phys.* **2007**, *127*, 134309.
(35) Mizukami, W.; Kurashige, Y.; Yanai, T. *J. Chem. Theory Comput.* **2012**, *7*, 401−407.
(36) Marti, K. H.; Ondík, I. M.; Moritz, G.; Reiher, M. *J. Chem. Phys.* **2008**, *128*, 014104.
(37) Kurashige, Y.; Chan, G. K.-L.; Yanai, T. *Nat. Chem.* **2013**, *5*, 660−666.
(38) Sharma, S.; Sivalingam, K.; Neese, F.; Chan, G. K.-L. *Nat. Chem.* **2014**, *6*, 927−933.
(39) Wouters, S.; Bogaerts, T.; Van Der Voort, P.; Van Speybroeck, V.; van Neck, D. *J. Chem. Phys.* **2014**, *140*, 241103.
(40) Kurashige, Y.; Yanai, T. *J. Chem. Phys.* **2009**, *130*, 234114.
(41) Fertitta, E.; Paulus, B.; Legeza, Ö. *Phys. Rev. B* **2014**, *90*, 245129.
(42) Yang, J.; Hu, W.; Usvyat, D.; Matthews, D.; Schütz, M. *Science* **2014**, *345*, 640−643.
(43) Knecht, S.; Legeza, Ö.; Reiher, M. *J. Chem. Phys.* **2014**, *140*, 041101.
(44) Liu, F.; Kurashige, Y.; Yanai, T.; Morokuma, K. *J. Chem. Theory Comput.* **2013**, *9*, 4462−4469.
(45) Pulay, P. *Mol. Phys.* **1969**, *17*, 197−204.
(46) Pulay, P. *Applications of Electronic Structure Theory*; Schaefer, H. F., III, Ed.; Springer: Boston, 1977; pp 153−185.
(47) Pulay, P. *Theor. Chem. Acc.* **1979**, *50*, 299−312.
(48) Pulay, P.; Fogarasi, G.; Pang, F.; Boggs, J. E. *J. Am. Chem. Soc.* **1979**, *101*, 2550−2560.
(49) Bérces, A.; Dickson, R. M.; Fan, L.; Jacobsen, H.; Swerhone, D.; Ziegler, T. *Comput. Phys. Commun.* **1997**, *100*, 247−262.
(50) Yamaguchi, Y., Goddard, J. D., Osamura, Y., Schaefer, H. F. *A New Dimension to Quantum Chemistry: Analytic Derivative Methods in Ab Initio Molecular Electronic Structure Theory*; Oxford University Press: New York, 1994.
(51) Rice, J. E.; Amos, R. D.; Handy, N. C.; Lee, T. J.; Schaefer, H. F., III. *J. Chem. Phys.* **1986**, *85*, 963−968.
(52) Shepard, R.; Lischka, H.; Szalay, P.; Kovar, T.; Ernzerhof, M. *J. Chem. Phys.* **1992**, *96*, 2085−2098.
(53) Lischka, H.; Dallos, M.; Shepard, R. *Mol. Phys.* **2002**, *100*, 1647−1658.
(54) Prochnow, E.; Evangelista, F. A.; Schaefer, H. F., III; Allen, W. D.; Gauss, J. *J. Chem. Phys.* **2009**, *131*, 064109.
(55) Jagau, T.-C.; Prochnow, E.; Evangelista, F. A.; Gauss, J. *J. Chem. Phys.* **2010**, *132*, 144110.
(56) Su, W.; Schrieffer, J.; Heeger, A. J. *Phys. Rev. Lett.* **1979**, *42*, 1698.
(57) Su, W.-P.; Schrieffer, J.; Heeger, A. *Phys. Rev. B* **1980**, *22*, 2099.
(58) Subbaswamy, K.; Grabowski, M. *Phys. Rev. B* **1981**, *24*, 2168.

(59) Boudreaux, D.; Chance, R.; Bredas, J.; Silbey, R. *Phys. Rev. B* **1983**, *28*, 6927.

(60) Soos, Z.; Ramasesha, S. *Phys. Rev. Lett.* **1983**, *51*, 2374.

(61) Aoyagi, M.; Osamura, Y.; Iwata, S. *J. Chem. Phys.* **1985**, *83*, 1140−1148.

(62) Hayden, G.; Mele, E. *Phys. Rev. B* **1986**, *34*, 5484.

(63) Tavan, P.; Schulten, K. *Phys. Rev. B* **1987**, *36*, 4337.

(64) Bredas, J.; Toussaint, J. *J. Chem. Phys.* **1990**, *92*, 2624−2629.

(65) Serrano-Andrés, L.; Merchán, M.; Nebot-Gil, I.; Lindh, R.; Roos, B. O. *J. Chem. Phys.* **1993**, *98*, 3151−3162.

(66) Hirao, K.; Nakano, H.; Nakayama, K.; Dupuis, M. *J. Chem. Phys.* **1996**, *105*, 9227−9239.

(67) Shuai, Z.; Bredas, J.; Pati, S.; Ramasesha, S. *Proc. SPIE* **1997**, *3145*, 293−302.

(68) Nakayama, K.; Nakano, H.; Hirao, K. *Int. J. Quantum Chem.* **1998**, *66*, 157−175.

(69) Fano, G.; Ortolani, F.; Ziosi, L. *J. Chem. Phys.* **1998**, *108*, 9246.

(70) Yaron, D.; Moore, E.; Shuai, Z.; Bredas, J. *J. Chem. Phys.* **1998**, *108*, 7451.

(71) Boman, M.; Bursill, R. *Synth. Met.* **1997**, *85*, 1059−1060.

(72) Barford, W.; Bursill, R. J.; Lavrentiev, M. Y. *J. Phys.: Condens. Matter* **1998**, *10*, 6429.

(73) Bursill, R. J.; Barford, W. *Phys. Rev. Lett.* **1999**, *82*, 1514.

(74) Barford, W.; Bursill, R. J.; Lavrentiev, M. Y. *Phys. Rev. B* **2001**, *63*, 195108.

(75) Barford, W.; Bursill, R. J.; Smith, R. W. *Phys. Rev. B* **2002**, *66*, 115205.

(76) Barford, W. *Phys. Rev. B* **2002**, *65*, 205118.

(77) Barford, W.; Bursill, R. J.; Lavrentiev, M. Y. *Phys. Rev. B* **2002**, *65*, 075107.

(78) Race, A.; Barford, W.; Bursill, R. J. *Phys. Rev. B* **2003**, *67*, 245202.

(79) Ma, H.; Liu, C.; Jiang, Y. *J. Chem. Phys.* **2004**, *120*, 9316−9320.

(80) Ma, H.; Cai, F.; Liu, C.; Jiang, Y. *J. Chem. Phys.* **2005**, *122*, 104909.

(81) Ma, H.; Liu, C.; Jiang, Y. *J. Chem. Phys.* **2005**, *123*, 084303.

(82) Ma, H.; Liu, C.; Jiang, Y. *J. Phys. Chem. B* **2006**, *110*, 26488−26496.

(83) Ma, H.; Schollwöck, U. *J. Chem. Phys.* **2008**, *129*, 244705.

(84) Ma, H.; Schollwock, U. *J. Phys. Chem. A* **2009**, *113*, 1360−1367.

(85) Ma, H.; Schollwock, U. *J. Phys. Chem. A* **2010**, *114*, 5439−5444.

(86) Barcza, G.; Legeza, Ö.; Gebhard, F.; Noack, R. M. *Phys. Rev. B* **2010**, *81*, 045103.

(87) Barcza, G.; Gebhard, F.; Legeza, Ö. *Mol. Phys.* **2013**, *111*, 2506−2515.

(88) Barcza, G.; Barford, W.; Gebhard, F.; Legeza, Ö. *Phys. Rev. B* **2013**, *87*, 245116.

(89) Barford, W. *Electronic and Optical Properties of Conjugated Polymers*; Oxford University Press, 2005.

(90) Dormans, G. J.; Groenenboom, G. C.; Buck, H. M. *J. Chem. Phys.* **1987**, *86*, 4895−4909.

(91) Olivucci, M.; Ragazos, I. N.; Bernardi, F.; Robb, M. A. *J. Am. Chem. Soc.* **1993**, *115*, 3710−3721.

(92) Celani, P.; Bernardi, F.; Olivucci, M.; Robb, M. A. *J. Chem. Phys.* **1995**, *102*, 5733−5742.

(93) Ito, M.; Ohmine, I. *J. Chem. Phys.* **1997**, *106*, 3159−3173.

(94) Ben-Nun, M.; Martínez, T. J. *Chem. Phys. Lett.* **1998**, *298*, 57−65.

(95) Brink, M.; Jonson, H.; Ottosson, C.-H. *J. Phys. Chem. A* **1998**, *102*, 6513−6524.

(96) Krawczyk, R. P.; Malsch, K.; Hohlneicher, G.; Gillen, R. C.; Domcke, W. *Chem. Phys. Lett.* **2000**, *320*, 535−541.

(97) Garavelli, M.; Smith, B. R.; Bearpark, M. J.; Bernardi, F.; Olivucci, M.; Robb, M. A. *J. Am. Chem. Soc.* **2000**, *122*, 5568−5581.

(98) Ostojić, B.; Domcke, W. *Contemp. Phys.* **2001**, *269*, 1−10.

(99) Garavelli, M.; Bernardi, F.; Olivucci, M.; Bearpark, M. J.; Klein, S.; Robb, M. A. *J. Phys. Chem. A* **2001**, *105*, 11496−11504.

(100) Sampedro Ruiz, D.; Cembran, A.; Garavelli, M.; Olivucci, M.; Fuß, W. *Photochem. Photobiol.* **2002**, *76*, 622−633.

(101) Dou, Y.; Torralva, B. R.; Allen, R. E. *J. Phys. Chem. A* **2003**, *107*, 8817−8824.

(102) Nonnenberg, C.; Grimm, S.; Frank, I. *J. Chem. Phys.* **2003**, *119*, 11585−11590.

(103) Köuppel, H.; Domcke, W.; Cederbaum, L. *Adv. Chem. Phys.* **2007**, *57*, 59−246.

(104) Levine, B. G.; Coe, J. D.; Martínez, T. J. *J. Phys. Chem. B* **2008**, *112*, 405−413.

(105) Levine, B. G.; Martínez, T. J. *J. Phys. Chem. A* **2009**, *113*, 12815−12824.

(106) Qu, Z.; Liu, C. *J. Chem. Phys.* **2013**, *139*, 244304.

(107) Levy, B.; Berthier, G. *Int. J. Quantum Chem.* **1968**, *2*, 307−319.

(108) Gerratt, J.; Mills, I. M. *J. Chem. Phys.* **1968**, *49*, 1719−1729.

(109) El Azhary, A.; Rauhut, G.; Pulay, P.; Werner, H.-J. *J. Chem. Phys.* **1998**, *108*, 5185−5193.

(110) Chan, G. K.-L. *Phys. Chem. Chem. Phys.* **2008**, *10*, 3454−3459.

(111) Dorando, J. J.; Hachmann, J.; Chan, G. K.-L. *J. Chem. Phys.* **2007**, *127*, 084109.

(112) White, S. R. *Phys. Rev. Lett.* **1992**, *69*, 2863−2866.

(113) Olivares-Amaya, R.; Hu, W.; Nakatani, N.; Sharma, S.; Yang, J.; Chan, G. K.-L. *J. Chem. Phys.* **2015**, *142*, 034102.

(114) Lee, C.; Yang, W.; Parr, R. G. *Phys. Rev. B* **1988**, *37*, 785.

(115) Balabanov, N. B.; Peterson, K. A. *J. Chem. Phys.* **2006**, *125*, 074110.

(116) Balabanov, N. B.; Peterson, K. A. *J. Chem. Phys.* **2005**, *123*, 64107.

(117) Dunning, T. H. *J. Chem. Phys.* **1989**, *90*, 1007.

(118) Werner, H.-J.; Knowles, P. J.; Knizia, G.; Manby, F. R.; Schütz, M. *Wiley Interdiscip. Rev.: Comput. Mol. Sci.* **2012**, *2*, 242−253.

(119) BLOCK Homepage. http://www.princeton.edu/chemistry/chan/software/dmrg/.

(120) Neese, F. The ORCA program system. *Wiley Interdiscip. Rev.: Comput. Mol. Sci.* **2012**, *2*, 73−78.

(121) Fletcher, R. *Comput. J.* **1970**, *13*, 317−322.

(122) Goldfarb, D. *Math. Comput.* **1970**, *24*, 23−26.

(123) Shanno, D. F. *Math. Comput.* **1970**, *24*, 647−656.

(124) Broyden, C. *Math. Comput.* **1967**, 368−381.

(125) Polívka, T.; Sundström, V. *Chem. Rev.* **2004**, *104*, 2021−2072.

(126) Kohler, B. E. *J. Chem. Phys.* **1988**, *88*, 2788−2792.

(127) Rohlfing, M.; Louie, S. G. *Phys. Rev. Lett.* **1999**, *82*, 1959.